

Article

Accelerating the Oxygen Reduction Reaction and Oxygen Evolution Reaction Activities of N and P Co-Doped Porous Activated Carbon for Li-O₂ Batteries

Hyun-Gi Jo  and Hyo-Jin Ahn * 

Department of Materials Science and Engineering, Seoul National University of Science and Technology, Seoul 01811, Korea; hgjo@seoultech.ac.kr

* Correspondence: hjahn@seoultech.ac.kr; Tel.: +82-02-970-6622

Received: 22 October 2020; Accepted: 12 November 2020; Published: 13 November 2020

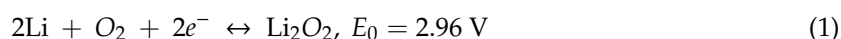


Abstract: Rechargeable lithium–oxygen (Li-O₂) batteries represent state-of-the-art electrochemical energy storage devices that provide high energy densities. However, their commercialization is challenging owing to their low charging/discharging efficiencies, short battery lives, high overpotentials, and high cathode manufacturing costs. In this study, we prepared a metal-free, N,P co-doped, porous activated carbon (N,P-PAC) electrode via KOH activation and P doping for application as a Li-O₂ battery cathode. When used in a rechargeable Li-O₂ battery, the N,P-PAC cathode showed a high specific discharge capacity (3724 mA h g⁻¹ at 100 mA g⁻¹), an excellent cycling stability (25 cycles with a limit capacity of 1000 mA h g⁻¹), and a low charge/discharge voltage gap (1.22 V at 1000 mA h g⁻¹). The N,P-PAC electrode showed a low overpotential (E_{OER-ORR}) of 1.54 V. The excellent electrochemical performance of the N,P-PAC electrode can mainly be attributed to its large active area and oxygen-containing functional groups generated via KOH activation and P-doping processes. Therefore, the N,P-PAC prepared in this study was found to be a promising eco-friendly and sustainable metal-free cathode material for Li-O₂ batteries.

Keywords: lithium–oxygen batteries; carbon; oxygen reduction reaction; oxygen evolution reaction; activation process; heteroatom co-doping

1. Introduction

Over the past few years, rechargeable non-aqueous lithium–oxygen (Li-O₂) batteries have gained immense attention as eco-friendly and sustainable energy storage devices for electric vehicle applications [1–3]. These batteries, especially those delivering a high energy density (3600 Wh kg⁻¹), are ideal candidates for use in long-distance electric vehicles [4]. Li-O₂ batteries consist of an O₂ cathode, a Li anode, a separator, and a non-aqueous lithium-ion conductive electrolyte in an oxygen atmosphere. The discharge and charge reactions of Li-O₂ batteries occur as follows:



The oxygen gas in the cathode reduces to Li₂O₂ through the oxygen reduction reaction (ORR) during the discharge process. Li₂O₂ then decomposes through the oxygen evolution reaction (OER) during the charging process [5]. However, Li₂O₂, which shows a high overpotential, does not decompose well between the electrolyte and cathode despite the large capacity of the Li₂O₂ reaction product. The cathode should possess a high electrical conductivity to decompose the Li₂O₂ reaction product and a large specific surface area to accommodate large amounts of the Li₂O₂ reaction product generated. Among the various

cathode materials investigated to date for rechargeable non-aqueous Li-O₂ batteries, carbon-based cathodes with high porosities, large surface areas, high conductivities, low costs, and light weights have been extensively investigated [6,7]. Furthermore, carbon-based O₂ cathodes have been actively developed to extend the cycle life of Li-O₂ batteries. To decrease the overpotential of carbon-based O₂ cathodes, various studies have been carried out focusing on the composition of noble metal catalysts (Pt, Ru, Pd, and Ir) and transition metal oxides (Co₃O₄, Fe₃O₄ and MnO₂) [8–10]. However, this method involves complicated processing and high production costs, thus hindering the commercialization of Li-O₂ batteries. Recently, carbon-based functional materials have emerged as promising catalysts or low-cost supports for catalysts in ORR and OER. Among these carbon-based materials, biomass-based carbon materials are promising candidates for use as supports for ORR and OER catalysts owing to their availabilities and low costs. For example, biomass-based carbon materials have been extracted from various biomaterials such as eggs, soybeans, plant shells, and chitin for application as ORR and OER catalysts [11–15].

In this study, tofu, which consists of protein, fat, and water, was used as the biomass material to prepare ORR and OER catalysts for Li-O₂ batteries. Tofu was carbonized in an inert atmosphere to obtain N-doped carbon (N-C) generated from amino acids, which improved the activity of the ORR and OER catalysts [16]. In addition, P doping of the activated carbon derived from tofu generated oxygen-containing functional groups, which affected the wettability between the electrolyte and electrode during cycling. Thus, the N,P co-doped porous activated carbon (N,P-PAC) was used as a bifunctional metal-free catalyst for the ORR and OER in high-performance Li-O₂ batteries.

2. Results and Discussion

2.1. Preparation and Morphological Properties

Figure 1 shows the procedure for the synthesis of N,P-PAC by carbonization through KOH activation and P doping. Protein-based tofu (Figure 1a), which contains amino acid and carboxyl groups, was carbonized at a temperature of 400 °C to synthesize N-doped carbon (N-C) (Figure 1b) [17]. The N-C obtained was crushed using planetary ball milling to form N-PAC (Figure 1c) via KOH activation. The KOH activation process for the formation of mesopores occurred as follows [18]:



Finally, N,P-PAC was obtained by carrying out P doping of N-PAC through high-temperature calcination (Figure 1d), which affected the ORR and OER performance of the N,P-PAC electrode.

Figure 2 shows the low- and high-resolution field-emission scanning electron microscopy (FE-SEM) images of the N-C, N-PAC, and N,P-PAC samples. The N-C sample showed a semi-block (~2.3–4.1 μm) and flat carbon surface with a small pore size of ~90.8–120 nm (Figure 2a,d). The N-PAC sample showed pores with a size of ~1.0 μm on the surface. These pores generated the KOH activation process (Figure 2b,e). The surface of the N,P-PAC sample was relatively rougher than the surfaces of the other samples investigated (Figure 2c,f). SEM images of Ketjenblack (K-B) showed a dense planar morphology with the particle size of ~0.1 μm (Figure S1). The highly porous surface of N,P-PAC can be attributed to the increased edge exposure of its carbon surface and active area due to the P-doping process [19,20]. To further investigate the morphology and structure of the N,P-PAC sample, transmission electron microscopy (TEM) and TEM-energy dispersive X-ray spectroscopy (EDS) analyses were carried out.

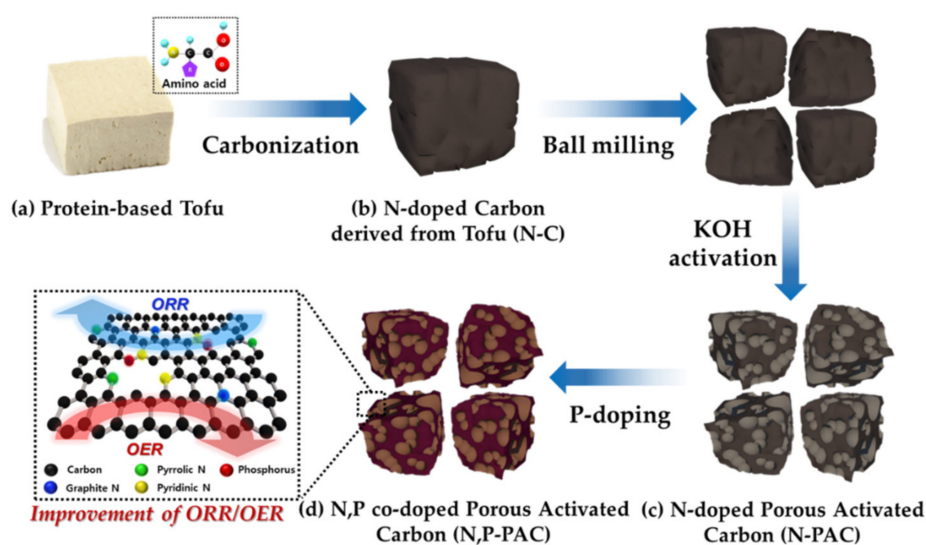


Figure 1. Schematic illustration of the procedure for the synthesis of N,P-PAC. (a) Protein-based tofu, (b) N-doped carbon derived from tofu (N-C), (c) N-doped porous activated carbon (N-PAC), and (d) N,P co-doped porous activated carbon (N,P-PAC).

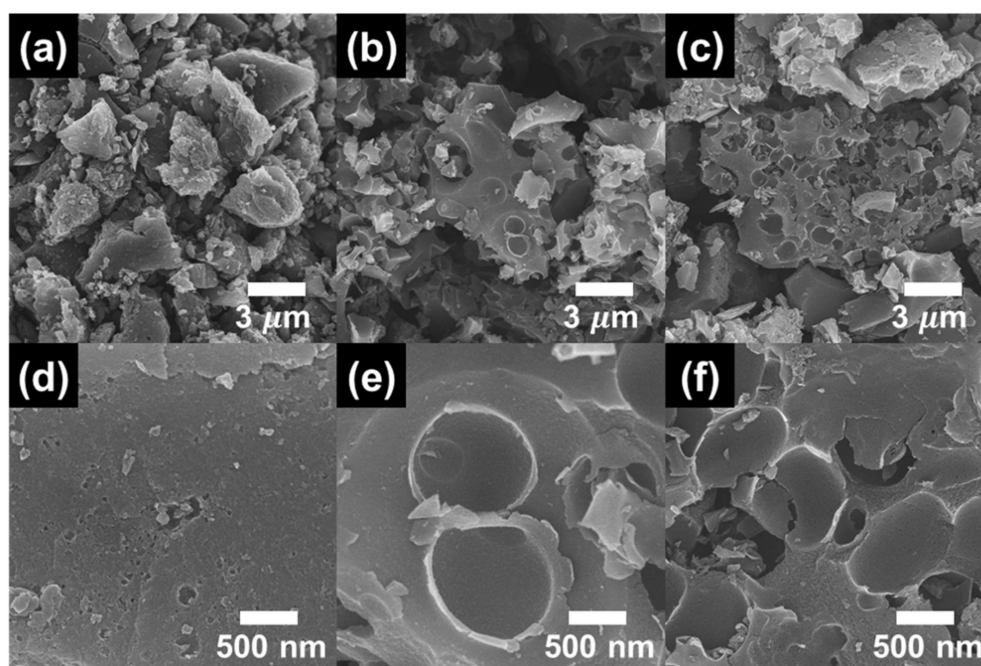


Figure 2. (a–c) Low- and (d–f) high-resolution field-emission scanning electron microscopy (FE-SEM) images of N-C, N-PAC, and N,P-PAC.

2.2. Structural and Chemical Properties

Figure 3 shows the low-resolution and high-resolution TEM images and TEM-EDS mapping results of the N,P-PAC sample. As can be observed from Figure 3a, the sample showed a porous structure with uniform contrast and consisted of a single carbon phase. The magnified high-resolution TEM image of the sample showed that segmental graphitization occurred during high-temperature calcination because of the increased adsorption of O_2 due to the increase in the number of active sites (Figure 3b) [16]. In addition, the selected area electron diffraction (SAED) patterns shown in Figure 3b confirm the amorphous characteristics of the N,P-PAC sample. The porous structure of

the sample with doped heteroatoms on the carbon surface improved its ORR and OER activities by increasing the number of active sites and functional groups on the carbon surface [21]. In addition, the TEM-EDS mapping results showed that C, N, and P were homogeneously distributed on the surface of the N,P-PAC sample, indicating the successful N, P co-doping of the PAC (Figure 3c).

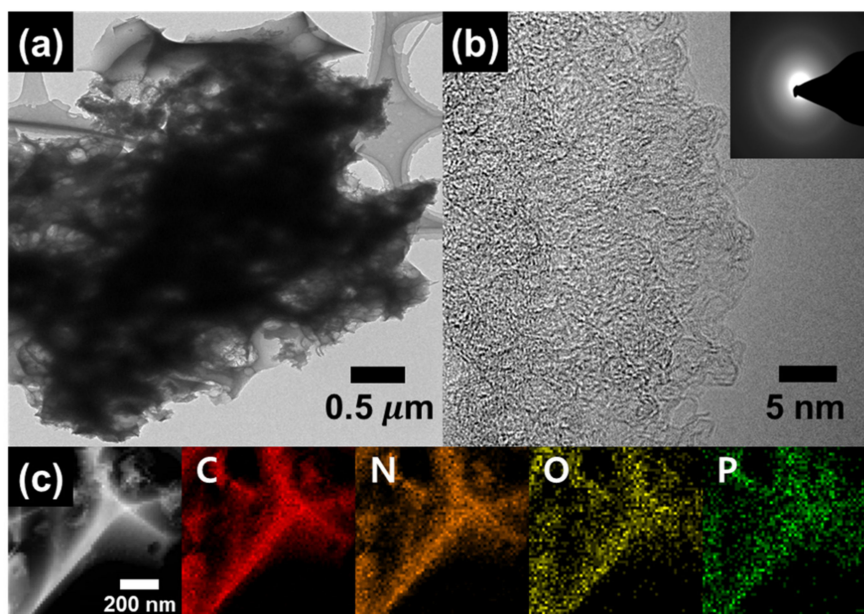


Figure 3. (a) Low- and (b) high-resolution transmission electron microscopy (TEM) images and (c) TEM-energy dispersive X-ray spectroscopy (EDS) mapping images obtained from the N,P-PAC.

Figure 4 shows the specific surface areas and pore structures of the samples, as obtained by the Brunauer–Emmett–Teller (BET) and Barrett–Joyner–Halenda (BJH) measurements. The samples showed different N_2 adsorption/desorption isotherms depending on their pore sizes: <2 nm (micropores), 2–50 nm (mesopores), and >50 nm (macropores) [22]. In Figure 4a, the N-C sample shows a Type I BET isotherm with a bulk structure with only micropores. However, the N-PAC and N,P-PAC samples exhibited type IV isotherms, indicating the presence of mesopores at high N_2 pressures ($P/P_0 > 0.4$) [23]. Figure 4b shows the pore volumes and pore diameter distributions of all the samples, as obtained via the BJH measurements. In particular, the N,P-PAC sample showed the highest pore volume with a mesopore diameter of 2–50 nm. This can be attributed to the formation of mesopores and surface defects due to carbon pyrolysis during the KOH activation and P doping processes. Figure 4c shows the specific surface areas and total pore volumes of the samples. The specific surface areas and pore volumes of the N-C, N-PAC, and N,P-PAC samples were $117.99 \text{ m}^2 \text{ g}^{-1}$ and $0.19 \text{ cm}^3 \text{ g}^{-1}$, $2086.6 \text{ m}^2 \text{ g}^{-1}$ and $1.22 \text{ cm}^3 \text{ g}^{-1}$, and $2473.3 \text{ m}^2 \text{ g}^{-1}$ and $1.53 \text{ cm}^3 \text{ g}^{-1}$, respectively [24]. Table 1 summarizes the BET and BJH results of the N-C, N-PAC, and N,P-PAC samples. The specific surface area of N-C ($117 \text{ m}^2 \text{ g}^{-1}$) increased significantly after KOH activation ($2086 \text{ m}^2 \text{ g}^{-1}$) and P doping ($2473 \text{ m}^2 \text{ g}^{-1}$). In the case of the N-PAC and N,P-PAC samples, the increase in the porosity and specific surface area due to the KOH activation process generated active sites for the formation of reaction products (Li_2O_2) [25]. In addition, the total pore volume and average pore diameter of N,P-PAC were $0.31 \text{ cm}^3 \text{ g}^{-1}$ and 0.14 nm higher than those of N-PAC, respectively. The pore size distribution (V_{meso}) of N,P-PAC was 5% higher than that of N-PAC. This could be attributed to the generation of additional oxygen-containing functional groups and defects on the carbon surface because of the P doping process in the case of the N,P-PAC sample [26]. The X-ray diffraction (XRD) patterns of the N-C, N-PAC, and N,P-PAC samples are shown in Figure S2. All the samples exhibited wide peaks at approximately $2\theta = 25^\circ$ corresponding to the (002) reflection planes of graphite (JCPDS card no. 41-1487) [27,28]. These peaks were observed within the 2θ range of $10\text{--}30^\circ$ in the case of the N-PAC and N,P-PAC

samples because of the continuous scattering of the X-ray radiation by the pores present in these samples [29].

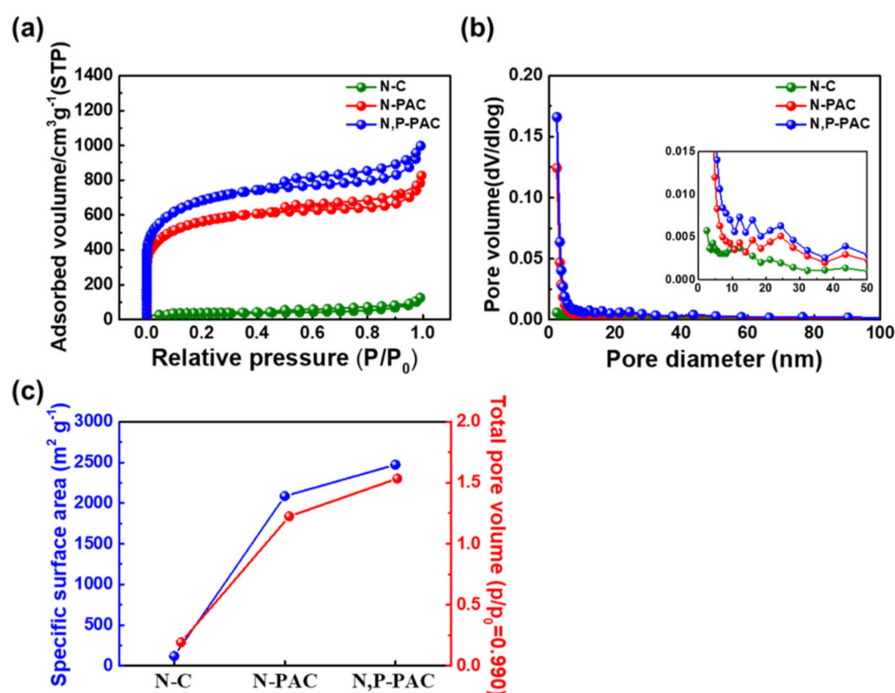


Figure 4. (a) N₂ adsorption/desorption Brunauer–Emmett–Teller (BET) isotherms, (b) Barrett–Joyner–Halenda (BJH) pore volumes and pore diameter distributions between 0.2 and 200 nm, and (c) the specific surface area and total pore volume from N-C, N-PAC and N,P-PAC.

Table 1. Brunauer–Emmett–Teller (BET) and Barrett–Joyner–Halenda (BJH) results of N-C, N-PAC, and N,P-PAC samples.

Samples	S_{BET} (m ² g ⁻¹)	Total Pore Volume (p/p ₀ = 0.990) (cm ³ g ⁻¹)	Average Pore Diameter (nm)	Pore Size Distribution	
				V_{micro} (%)	V_{meso} (%)
N-C	117	0.19	6.53	-	-
N-PAC	2086	1.22	2.34	60%	40%
N,P-PAC	2473	1.53	2.48	55%	45%

To further analyze the chemical bonding states of N,P-PAC, X-ray photoelectron spectroscopy (XPS) measurements were carried out, as shown in Figure 5. The C 1s peak of N,P-PAC could be deconvoluted into different peaks corresponding to the C–C (284.5 eV), C–N and C–P (285.4 eV), C–O (286.6 eV), and N=C–O (289.6 eV) groups (Figure 5a). The peaks corresponding to the C–N and C–P groups (285.4 eV) indicate the replacement of C atoms with N or P atoms in the C–C bonds [30]. Figure 5b shows the O 1s XPS spectra of N,P-PAC. The O 1s peak could be deconvoluted into four peaks corresponding to the C–O and P–O (531.2 eV), –OH (532.2 eV), O=C=O (532.9 eV), and –COOH (535.4 eV) groups. The peak corresponding to C–O bonds indicates that most of the oxygen-containing groups on the carbon lattice were formed by high-temperature calcination. The P–O peak indicates the chemical adsorption of oxygen onto the surface of N,P-PAC [31]. Moreover, the oxygen-containing functional groups (–O, –OH, and =O) generated on the carbon surface via P-doping reduced the charge/discharge overpotential of the electrode by facilitating the accessibility of charges and by improving the wettability of the electrode and electrolyte. Figure 5c shows the N 1s XPS spectra of N,P-PAC. The N 1s peak of the sample could be deconvoluted into peaks corresponding to pyridinic-N (398.7 eV), pyrrolic-N (400.0 eV), and graphitic-N (401.1 eV). The pyridine-N and pyrrole-N in this sample were derived from the amino acids present in the protein-based tofu. These N groups were generated by breaking the carbon lattice

and providing one and two p-electrons, respectively, through an aromatic π system [14,26]. Figure 5d shows the P 2p XPS spectra of N,P-PAC. The P 2p peak of N,P-PAC could be deconvoluted into two peaks corresponding to the P–C (132.8 eV) and P–O (134.3 eV) groups. The presence of covalent P–C bonds indicates that the P atoms were doped at the edges of the graphite layer at temperatures higher than 700 °C [32]. The doped P atoms caused the charge delocalization of the sp^2 -carbon lattice, thereby increasing the electrical conductivities of the adjacent C atoms. The P–O bond states were formed at the edges of the graphite lattice by oxygen-containing functional groups. In addition, the ratio of the peak areas of the P–C and P–O bonds was close to 1:1, indicating the successful doping of P atoms into the carbon lattice. The activated functional groups generated by the P-doping process improved the electrocatalytic performance of Li-O₂ battery cathodes for the ORR and OER [30–32]. Thus, the XPS results confirmed the successful formation of N,P-PAC.

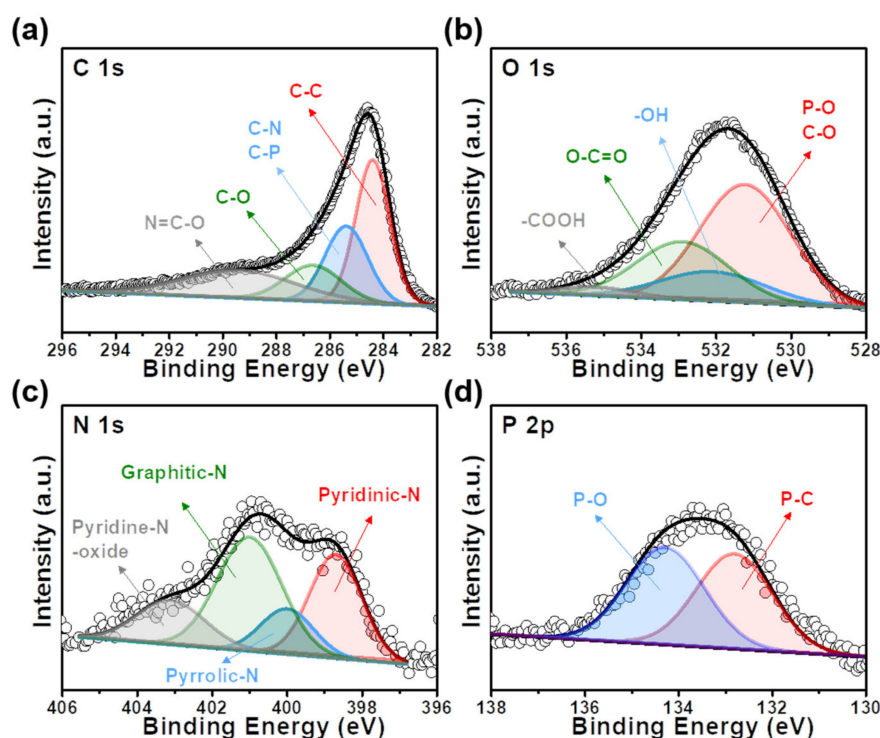


Figure 5. X-ray photoelectron spectroscopy (XPS) spectra results of (a) C 1s, (b) O 1s, (c) N 1s, and (d) P 2p for N,P-PAC.

2.3. Electrochemical Catalytic Properties

Figure 6 shows the discharge/charge profiles and cycling performances of the N-C, N-PAC, and N,P-PAC O₂ cathodes in Li-O₂ batteries. The first charge/discharge curves of the Ketjenblack (K-B), N-C, N-PAC, and N,P-PAC electrodes were obtained within the potential range of 2.0–4.5 V at a current density of 100 mA g^{−1} (Figure 6a). N,P-PAC exhibited a high first discharge-specific capacity (3724 mA h g^{−1}) as compared to those exhibited by K-B (2211 mA h g^{−1}), N-C (1885 mA h g^{−1}), and N-PAC (3018 mA h g^{−1}). The reversible charge capacity of N,P-PAC at the 1st cycle was 4936 mA h g^{−1} higher than those of K-B (2289 mA h g^{−1}), N-C (1885 mA h g^{−1}), and N-PAC (3572 mA h g^{−1}). In addition, in the first charge/discharge cycle, N-C showed a large charge/discharge voltage gap (1.77 V at 1000 mA h g^{−1}) between the ORR and OER curves, while N,P-PAC showed a relatively low charge/discharge voltage gap (1.22 V at 1000 mA h g^{−1}). In particular, the increase in the specific capacity (approximately 2000 mA h g^{−1}) and the decrease in the charge/discharge voltage gap (0.5V) improved the ORR and OER activities of N,P-PAC. This improvement in the performance of N,P-PAC can be attributed to the increase in the active area and number of functional groups via KOH activation and P-doping processes [33,34]. These results can be explained as follows: (I) the porous

activated carbon surface increased the active area for O_2 adsorption, improving the ORR catalytic activity of N,P-PAC. (II) P doping process generated a large number of oxygen-containing functional groups in the carbon lattice structure, which in turn improved the OER. Accordingly, the N,P-PAC electrode retained a high charge/discharge specific capacity owing to its low charge/discharge voltage gap. Figure 6b shows the cycle performances of the K·B, N-C, N-PAC, and N,P-PAC electrodes measured over the potential range of 2.0–4.5 V at a current density of 100 mA g^{-1} under the specific capacity limit of 1000 mA h g^{-1} . The K·B, N-C, N-PAC, and N,P-PAC electrodes exhibited stable charge/discharge capacities over 18, 11, 22, and 25 cycles, respectively. Thereafter, the electronic conductivity of the oxygen electrodes decreased because of the accumulation of Li_2O_2 on the electrode surface, which deteriorated the ORR and OER properties of all the samples, resulting in a rapid decrease in their specific capacities [35]. Figure 6c–f show the capacity-limited charge/discharge profiles of the samples at the 1st, 5th, 10th, 15th, 20th, and 25th cycles over the potential range of 2.0–4.5 V at a current density of 100 mA g^{-1} . In addition, the charge/discharge curves of all the electrodes over 30 cycles are shown in Figure S3. As can be observed from Figure 6c, the K·B electrode remains stable over the first five cycles. However, the ORR-OER overpotential gradually increases after 10 cycles, resulting in a rapid capacity decrease after 15 cycles. In the case of the N-C electrode (Figure 6d), the ORR-OER overpotential decreased more rapidly after the first five cycles. This was because the decomposition of the Li_2O_2 product did not occur continuously in the N-C electrode owing to its small active area. In addition, the capacity maintenance at a specific capacity limit of 1000 mA h g^{-1} terminated before 12 cycles. [36]. In contrast, the N-PAC electrode exhibits stable ORR and OER activities for a cycle retention up to 15 cycles because of the increased active carbon surface due to KOH activation [25]. After 20 cycles, the N-PAC electrode shows a slow capacity drop compared to the N-C electrode (Figure 6e) [37]. As can be observed from Figure 6f, the N,P-PAC electrode show the lowest ORR-OER overpotential and the most stable cycling performance up to 25 cycles among all the samples investigated. This can be attributed to the increases in the active area and the number of oxygen-containing functional groups of N,P-PAC due to KOH activation and P-doping processes. Thus, the N,P-PAC electrode showed excellent ORR and OER catalytic activities for application in $Li-O_2$ batteries. To further evaluate the ohmic resistance of the K·B, N-C, N-PAC, and N,P-PAC electrodes related to their charge/discharge reversibilities during cycling, their voltage (V) vs. time (h) profiles were obtained (Figure S4). The discharge voltage drop of an electrode during cycling is directly related to its cycling stability [38]. The N,P-PAC electrode maintained its charge/discharge voltage over the potential range of 2.0–4.5 V for up to 500 h (~25 cycles). This can be attributed to the presence of a large number of active sites and oxygen-containing functional groups (-O, =O, and -OH), which improved the reversibility of the formation and decomposition of the reaction product (Li_2O_2) because of the improved wettability between the electrolyte and electrode [24,39]. The K·B, N-C, and N-PAC electrodes maintained their charge/discharge voltages up to 350 (~17 cycles), 220 (~11cycles), and 450 h (~22 cycles), respectively. Thus, the N,P-PAC electrode exhibited an excellent cycling performance as compared to the other samples. This was consistent with the results obtained from the voltage (V) vs. specific capacity (mA h g^{-1}) and specific capacity (mA h g^{-1}) vs. cycle number (n) profiles of the samples. To further investigate the ORR and OER performances of the electrodes, their cyclic voltammetry (CV) and linear sweep voltammetry (LSV) measurements were carried out, as shown in Figure 7.

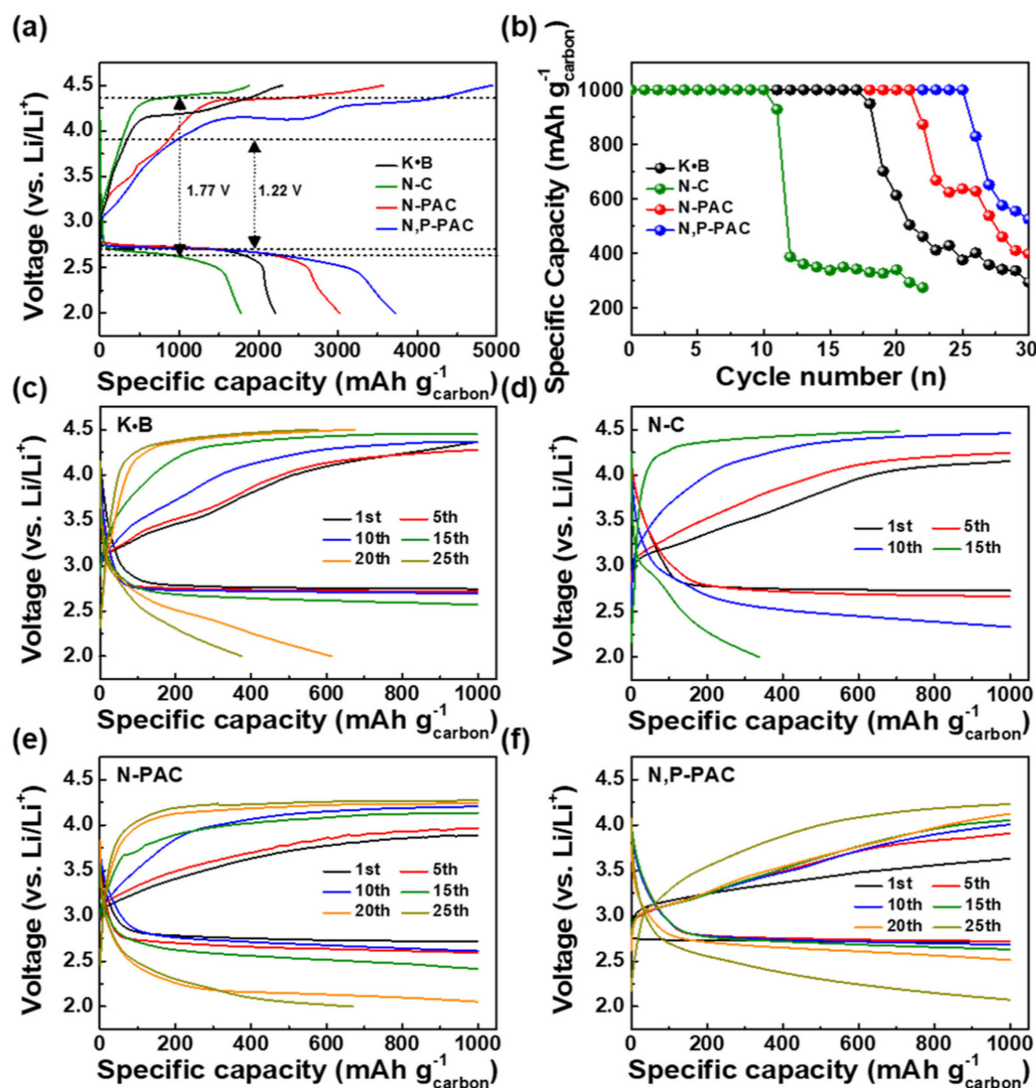


Figure 6. (a) Initial charge/discharge profiles of Ketjenblack (K·B), N-C, N-PAC, and N,P-PAC electrodes were obtained within the potential range of 2.0–4.5 V at the current density of 100 mA g^{-1} , (b) cycle performances of K·B, N-C, N-PAC, and N,P-PAC electrodes measured over the potential range of 2.0–4.5 V at the current density of 100 mA g^{-1} under the specific capacity limit of 1000 mA h g^{-1} , (c) K·B, (d) N-C, (e) N-PAC, and (f) N,P-PAC electrodes capacity-limited charge/discharge profiles at the 1st, 5th, 10th, 15th, 20th, and 25th cycles over the potential range of 2.0–4.5 V at the current density of 100 mA g^{-1} .

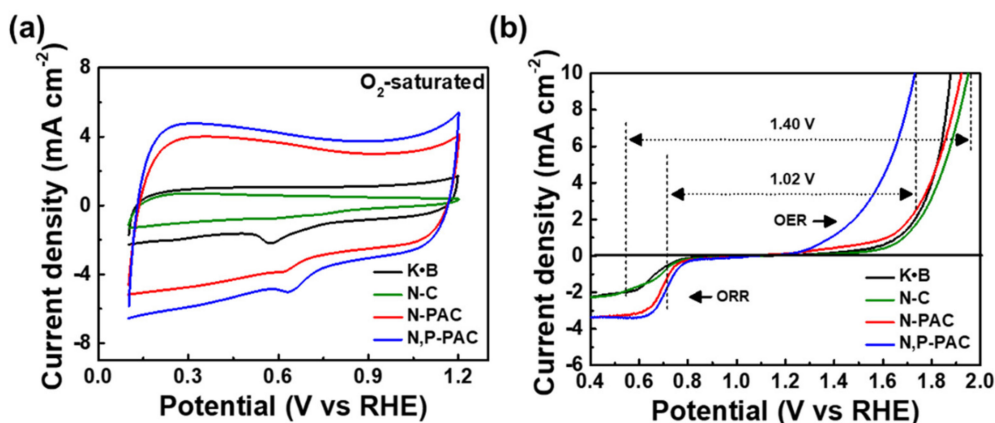


Figure 7. (a) Cyclic voltammetry (CV) curves of K·B, N-C, N-PAC, and N,P-PAC electrodes obtained at the scan rate of 50 mV s^{-1} in O_2 -saturated 0.1 M KOH electrolyte, (b) oxygen reduction reaction (ORR) and oxygen evolution reaction (OER) electrocatalytic activities of K·B, N-C, N-PAC, and N,P-PAC electrodes obtained at the scan rate of 5 mV s^{-1} in O_2 -saturated 0.1 M KOH electrolyte using a rotating disk electrode (RDE) at the rotational speed of 1600 rpm.

Figure 7a shows the CV curves of the K·B, N-C, N-PAC, and N,P-PAC electrodes obtained at a scan rate of 50 mV s^{-1} in an O_2 -saturated 0.1 M KOH electrolyte. All samples exhibit electric double layer curves typical of carbon materials. The N,P-PAC electrode shows the largest voltage current area, and hence the largest electrochemical reaction active area [40]. In addition, the N,P-PAC electrode showed a distinct oxygen reduction peak at 0.632 V as compared to the K·B (0.571 V), N-C (0.576 V), and N-PAC (0.618 V) electrodes. In the case of N-C, the smallest electric double layer and two cathodic peaks (at 0.576 and 0.740 V) were observed. These results can be related to the surface area, morphology, and pore size distribution of the active materials [41]. N,P-PAC exhibited a high S_{BET} of $2473 \text{ m}^2 \text{ g}^{-1}$, presenting a large total pore volume of $1.53 \text{ cm}^3 \text{ g}^{-1}$, and mesopore volume fraction (Table 1). On the other hand, N-C showed a semi-block morphology with low S_{BET} of $117 \text{ m}^2 \text{ g}^{-1}$ and small total pore volume of $0.19 \text{ cm}^3 \text{ g}^{-1}$. This can be attributed to the porous and heteroatom co-doped carbon surface of the N,P-PAC electrode [42,43]. To further evaluate the oxygen reaction activities of the electrodes, their LSV measurements were carried out. The ORR and OER electrocatalytic activities of the electrodes were evaluated using a rotating disk electrode (RDE) at a rotational speed of 1600 rpm in an O_2 -saturated 0.1 KOH electrolyte (Figure 7b). In the region of the ORR polarization curve, N,P-PAC shows an improved onset potential (E_{onset}) of $\sim 0.80 \text{ V}$ and half-wave potential ($E_{1/2}$) of $\sim 0.71 \text{ V}$ compared to other samples (Figure S5). In addition, in the OER polarization curves, the N,P-PAC electrode shows the most negative OER onset potential among them, suggesting that N, P-PAC is an excellent OER catalyst. The Tafel plots of N,P-PAC (137 mV dec^{-1}) are lower than that of K·B (187 mV dec^{-1}), N-C (193 mV dec^{-1}), N,P-PAC (160 mV dec^{-1}) in the ORR performance (Figure S6a). Likewise, N,P-PAC shows lower Tafel plots (206 mV dec^{-1}) compared to K·B (245 mV dec^{-1}), N-C (258 mV dec^{-1}), and N-PAC (268 mV dec^{-1}) in the OER performance (Figure S6b). This indicates that N,P-PAC has favorable ORR and OER kinetics [44]. During the charging/discharging process of Li-O₂ batteries, the ORR and OER are very important for operation, and electrochemical kinetics are generally evaluated as the potential gap ($E_{\text{OER-ORR}}$) between the ORR (at -2 mA cm^{-2}) and OER (at 10 mA cm^{-2}) [45]. The N,P-PAC electrode shows a potential gap ($E_{\text{OER-ORR}}$) of 1.02 V, which is significantly lower than those of the K·B (1.32 V), N-C (1.40 V), and N-PAC (1.23 V) electrodes. This was because of the increased ORR and decreased OER potentials of the N,P-PAC electrode, resulting from an increase in its active area and number of oxygen-containing functional groups. Thus, the N,P-PAC electrode with reversible oxygen reaction activity can be used as an O_2 cathode for the development of high-performance Li-O₂ batteries.

3. Materials and Methods

3.1. Experimental Details

The tofu used to produce carbon in this study was purchased from Pulmuone Co., Ltd. (Seoul, Korea) and dried at 80 °C for 12 h in an oven to remove any moisture. The dried tofu was pyrolyzed at 400 °C for 2 h in air to eliminate impurities. The pyrolyzed carbon derived from the tofu was crushed via planetary ball milling at 600 rpm for 12 h in ethanol. The pyrolyzed carbon was then carbonized at 800 °C for 2 h in an N₂ atmosphere to produce N-doped carbon (N-C). To prepare porous carbon, the pyrolyzed carbon was mixed with potassium hydroxide (KOH, SAMCHUN, 85.0%) at a weight ratio of 4:1 ($W_{\text{KOH}}/W_{\text{carbon}}$) and was then carbonized at 800 °C for 2 h under an N₂ atmosphere to produce N-PAC. The N-PAC obtained was washed several times with deionized water and dried at 80 °C for 12 h in an oven. Finally, the prepared sample was stirred with phosphorus red (P₄, Aladdin, 98.5%) for additional P doping, followed by high-temperature calcination at 800 °C for 4 h in an N₂ atmosphere. Therefore, N,P-PAC was successfully prepared.

3.2. Characterization

3.2.1. Structures and Morphologies

The morphologies and structures of the samples were analyzed using field-emission scanning electron microscopy (FE-SEM, Hitachi S-4800, Korea University) and transmission electron microscopy (TEM, MULTI/TEM; Tecnai G², KBSI Gwangju Center). TEM-EDS (Philips CM20T/STEM, KBSI Gwangju Center) was used to analyze the elemental distribution of the samples. The specific surface areas, pore diameters, and pore volumes of the samples were determined using the BET and BJH methods from their N₂ adsorption isotherms (77 K). The crystal structures of the samples were examined using XRD (Rigaku D/Max-2500 diffractometer using Cu K_α radiation, Chonnam National University) over the range of 10–90° with a step size of 0.02°. The chemical bonding states of the samples were analyzed via XPS (ESCALAB 250 equipped with an Al K_α X-ray source, Chonnam National University). All the XPS data were standardized to the C 1s core level (284.5 eV).

3.2.2. Electrochemical Measurements

Electrochemical measurements of all the samples were carried out using a metal-O₂ battery coin cell (CR2032, Hohsen Corporation), which was composed of a Li metal foil (Honjo Chemical, 99.8%) as the anode, a 1.0 M lithium bis(trifluoromethanesulfonyl)imide (LiTFSI) in tetraethylene glycol dimethyl ether (TEGDME) solution as the electrolyte, a porous polypropylene membrane (Celgard 2400) as the separator, and a carbon electrode as the cathode. The O₂ cathode electrode was fabricated using a mixture of active materials (N-C, N-PAC, and N,P-PAC), poly(vinylidenedifluoride) (PVDF, Alfa Aesar) as the binder, and Ketjenblack (K-B, ECP-600JD, Mitsubishi Chemical, Tokyo, Japan) as the conducting material. These were dissolved in a weight ratio of 7:2:1 in N-methyl-2-pyrrolidinone (NMP, Aldrich, St. Louis, USA) and the resulting mixture was spray coated onto a Ni substrate (Nickel foam, MTI Korea, Seoul, Korea), which acted as the current collector. The O₂ cathodes obtained were dried in an oven at 80 °C for 12 h. The catalyst loading of the electrodes was 1 mg ± 0.1 mg, except for the Ni substrate (Figure S7a,b). All the Li-O₂ coin cells were assembled in a high-purity (99.999%) argon-filled glove box, in which the H₂O and O₂ contents were controlled to less than 10 ppm (Figure S7c). The assembled cells were aged for 1 h in an O₂-filled case prior to battery testing. To investigate the electrochemical performance of the prepared O₂ cathode, discharge–charge tests were performed using a battery cycler system (WBCS3000S, WonATech, Seoul, Korea) over the potential range of 2.0–4.5 V (vs. Li/Li⁺) at 25 °C in an O₂-filled case. The cycling stabilities of the electrodes were evaluated for up to 50 cycles at a current density of 100 mA g⁻¹ with a limit capacity of 1000 mA h g⁻¹ with a limited *Gravimetric-specific*

capacity of 1000 mA h g⁻¹ (Area-specific capacity of 0.75 mA h cm⁻²) (Figure S8). The calculation of the area-specific capacity was derived by the following equation [46]:

$$\text{Area of electrode} = \frac{6.5^2 \text{ mm} \times \pi}{100} \approx 1.32 \text{ cm}^2 \quad (5)$$

$$\text{Area-specific capacity (mAh cm}^{-2}\text{)} = \text{Gravimetric specific capacity (mAh g}^{-1}\text{)} \times \frac{0.001 \text{ g}}{1.32 \text{ cm}^2} \quad (6)$$

To measure the ORR and OER activities of the electrodes, a potentiostat/galvanostat (PGST302N, Eco Chemie Autolab, Utrecht, Netherlands) with an RDE and a rotating ring-disk electrode (RRDE) was used. The three-electrode system used for the electrochemical measurements was composed of a counter electrode (Pt wire), a reference electrode (Ag/AgCl, sat. KCl), and the working electrode (glassy carbon). All the potentials in this measurement were converted by reference to the reversible hydrogen electrode (RHE) using the following conversion equation [47,48]:

$$E_{\text{RHE}} = E_{\text{Ag/AgCl}} + E_{\text{Ag/AgCl}}^0 + 0.059 \times \text{pH} \left(E_{\text{Ag/AgCl}}^0 = +0.197 \text{ V} \right) \quad (7)$$

Catalyst inks were prepared using a mixture of 80 wt% of the carbon electrocatalysts (N,P-PAC) and 20 wt% Nafion (Aldrich, St. Louis, USA) in 2-propanol (Aldrich, St. Louis, USA) followed by dispersion for three days. All the catalyst inks were carefully loaded on the working electrode, which was then dried in an oven at 50 °C. CV and LSV measurements were carried out at scan rates of 50 and 5 mV s⁻¹ with a rotational speed of 1600 rpm in an O₂-saturated 0.1 M KOH electrolyte.

4. Conclusions

N,P-PAC derived from protein-based tofu was successfully prepared via KOH activation and P doping. The N,P-PAC electrode exhibited high specific discharge capacity (3724 mA h g⁻¹ at 100 mA g⁻¹), a low charge/discharge voltage gap (1.22 V at 1000 mA h g⁻¹) between the ORR and OER, and an excellent cycling stability (25 cycles with a limit capacity of 1000 mA h g⁻¹). The excellent electrochemical performance of the N,P-PAC electrode can be explained by the following factors: (i) the N-doped carbon fabricated using the amino acids extracted from the protein-based tofu increased the amount of electron distribution on the electrode; (ii) the increased surface area obtained via KOH activation could accommodate the large amount of the reaction product (Li₂O₂), leading to an increase in the specific capacity of the electrode; and (iii) the oxygen-containing functional groups generated by P doping improved the ORR and OER catalytic activities of the electrode. Thus, the N,P-PAC electrode was found to be suitable for improving the electrochemical oxygen catalytic performance of Li-O₂ batteries.

Supplementary Materials: Supplementary materials can be found at <http://www.mdpi.com/2073-4344/10/11/1316/s1>. Figure S1. Low- and high-resolution FESEM images of K-B, Figure S2. XRD patterns of K-B, N-C, N-PAC, and N,P-PAC, Figure S3. (a) K-B, (b) N-C, (c) N-PAC, and (d) N,P-PAC electrodes capacity-limited charge/discharge profiles over 30 cycles for the potential range of 2.0–4.5 V at a current density of 100 mA g⁻¹, Figure S4. Ohmic resistance of the (a) K-B, (b) N-C, (c) N-PAC, and (d) N,P-PAC electrodes related to their charge/discharge reversibilities during cycling, their voltage (V) vs. time (h) profiles over the potential range of 2.0–4.5 V for up to 500 h under a specific capacity limit of 1000 mA h g⁻¹, Figure S5. Comparison of onset potential (V vs. RHE) and the half-wave potential (V vs. RHE) of K-B, N-C, N-PAC, and N,P-PAC, Figure S6. (a) ORR and (b) OER Tafel plots of K-B, N-C, N-PAC, and N,P-PAC, Figure S7. Photograph of (a) bare Ni substrate, (b) N,P-PAC spray-coated air-cathode on Ni substrate, and (c) photograph and structure diagram of assembled cell, Figure S8. Cycle performances of K-B, N-C, N-PAC, and N,P-PAC electrodes measured over the potential range of 2.0–4.5 V at a current density of 100 mA g⁻¹ calculated according to (a) gravimetric-specific capacity and (b) area-specific capacity.

Author Contributions: Conceptualization, H.-G.J. and H.-J.A.; methodology, H.-G.J.; validation, H.-G.J. and H.-J.A.; formal analysis, H.-G.J. and H.-J.A.; investigation, H.-G.J.; resources, H.-J.A.; data curation, H.-G.J.; writing—original draft preparation, H.-G.J. and H.-J.A.; writing—review and editing, H.-G.J. and H.-J.A.; visualization, H.-G.J.; supervision, H.-J.A.; project administration, H.-J.A.; funding acquisition, H.-J.A. All authors have read and agreed to the published version of the manuscript.

Funding: This work was supported by the National Research Foundation of Korea (NRF) grant funded by the Korean government (MSIT) (No. 2019R1 A2 C1005836).

Conflicts of Interest: The authors declare no conflicts of interest.

References

1. Girishkumar, G.; McCloskey, B.; Luntz, A.C.; Swanson, S.; Wilcke, W. Lithium-Air Battery: Promise and Challenges. *J. Phys. Chem. Lett.* **2010**, *1*, 2193–2203. [[CrossRef](#)]
2. Geng, D.; Ding, N.; Hor, T.S.A.; Chien, S.W.; Liu, Z.; Wu, D.; Sun, X.; Zong, Y. From Lithium-Oxygen to Lithium-Air Batteries: Challenges and Opportunities. *Adv. Energy Mater.* **2016**, *6*, 1502164–1502177. [[CrossRef](#)]
3. Balaish, M.; Kraytsberg, A.; Ein-Eli, Y. A critical review on lithium-air battery electrolytes. *Phys. Chem. Chem. Phys.* **2014**, *16*, 2801–2822. [[CrossRef](#)] [[PubMed](#)]
4. Aurbach, D.; McCloskey, B.D.; Nazar, L.F.; Bruce, P.G. Advances in understanding mechanisms underpinning lithium-air batteries. *Nat. Energy* **2016**, *1*, 16128–16138. [[CrossRef](#)]
5. Lu, Y.-C.; Shao-Horn, Y. Probing the Reaction Kinetics of the Charge Reactions of Nonaqueous Li-O₂ Batteries. *J. Phys. Chem. Lett.* **2013**, *4*, 93–99. [[CrossRef](#)] [[PubMed](#)]
6. Huang, S.; Fan, W.; Guo, X.; Meng, F.; Liu, X. Positive Role of Surface Defects on Carbon Nanotube Cathodes in Overpotential and Capacity Retention of Rechargeable Lithium-Oxygen Batteries. *ACS Appl. Mater. Interfaces* **2014**, *6*, 21567–21575. [[CrossRef](#)] [[PubMed](#)]
7. Shui, J.; Lin, Y.; Connell, J.W.; Xu, J.; Fan, X.; Dai, L. Nitrogen-Doped Holey Graphene for High-Performance Rechargeable Li-O₂ Batteries. *ACS Energy Lett.* **2016**, *1*, 260–265. [[CrossRef](#)]
8. Ma, Z.; Yuan, X.; Li, L.; Ma, Z.-F.; Wilkinson, D.P.; Zhang, L.; Zhang, J. A review of cathode materials and structures for rechargeable lithium-air batteries. *Energy Environ. Sci.* **2015**, *8*, 2144–2198. [[CrossRef](#)]
9. Wen, Z.; Shen, C.; Lu, Y. Air Electrode for the Lithium-Air Batteries: Materials and Structure Designs. *ChemSusChem* **2015**, *8*, 270–287.
10. Han, S.J.; Ameen, M.; Hanifah, M.F.R.; Aqsha, A.; Bilad, M.R.; Jaafar, J.; Kheawhom, S. Catalytic Evaluation of Nanoflower Structured Manganese Oxide Electrocatalyst for Oxygen Reduction in Alkaline Media. *Catalysts* **2020**, *10*, 822–835.
11. Liu, X.; Zhou, Y.; Zhou, W.; Li, L.; Huang, S.; Chen, S. Biomass-derived nitrogen self-doped porous carbon as effective metal-free catalysts for oxygen reduction reaction. *Nanoscale* **2015**, *7*, 6136–6142. [[CrossRef](#)] [[PubMed](#)]
12. Yan, L.; Yu, J.; Houston, J.; Flores, N.; Luo, H. Biomass derived porous nitrogen doped carbon for electrochemical devices. *Green Energy Environ.* **2017**, *2*, 84–99. [[CrossRef](#)]
13. Zhang, G.; Yao, Y.; Zhao, T.; Wang, M.; Chen, R. From Black Liquor to Green Energy Resource: Positive Electrode Materials for Li-O₂ Battery with High Capacity and Long Cycle Life. *ACS Appl. Mater. Interfaces* **2020**, *12*, 16521–16530. [[CrossRef](#)] [[PubMed](#)]
14. Zhou, N.; Wang, N.; Wu, Z.; Li, L. Probing Active Sites on Metal-Free, Nitrogen-Doped Carbons for Oxygen Electroreduction: A Review. *Catalysts* **2018**, *8*, 509. [[CrossRef](#)]
15. Wang, M.; Ma, J.; Yang, H.; Lu, G.; Yang, S.; Chang, Z. Nitrogen and Cobalt Co-Doped Carbon Materials Derived from Biomass Chitin as High-Performance Electrocatalyst for Aluminum-Air Batteries. *Catalysts* **2020**, *9*, 954. [[CrossRef](#)]
16. An, G.-H.; Lee, D.-Y.; Ahn, H.-J. Tofu-derived carbon framework with embedded ultrasmall tin nanocrystals for high-performance energy storage devices. *J. Alloy. Compd.* **2017**, *722*, 60–68. [[CrossRef](#)]
17. An, G.-H.; Kim, H.; Ahn, H.-J. Surface functionalization of nitrogen-doped carbon derived from protein as anode material for lithium storage. *Appl. Surf. Sci.* **2019**, *463*, 18–26. [[CrossRef](#)]
18. Wang, J.; Kaskel, S. KOH activation of carbon-based materials for energy storage. *J. Mater. Chem.* **2012**, *22*, 23710–23725. [[CrossRef](#)]
19. Wu, J.; Yang, Z.; Sun, Q.; Li, X.; Strasser, P.; Yang, R. Synthesis and electrocatalytic activity of phosphorus-doped carbon xerogel for oxygen reduction. *Electrochim. Acta* **2014**, *127*, 53–60. [[CrossRef](#)]
20. Jiang, Z.-L.; Sun, H.; Shi, W.-K.; Cheng, J.-Y.; Hu, J.-Y.; Guo, H.-L.; Gao, M.-Y.; Zhou, H.; Sun, S.-G. P-Doped Hive-like Carbon Derived from Pinecone Biomass as Efficient Catalyst for Li-O₂ Battery. *ACS Sustainable Chem. Eng.* **2019**, *7*, 14161–14169. [[CrossRef](#)]
21. Zhao, Z.; Xia, Z. Design Principles for Dual-Element-Doped Carbon Nanomaterials as Efficient Bifunctional Catalysts for Oxygen Reduction and Evolution Reactions. *ACS Catal.* **2016**, *6*, 1553–1558. [[CrossRef](#)]

22. Kim, K.-H.; Shin, D.-Y.; Ahn, H.-J. Ecklonia cava based mesoporous activated carbon for high-rate energy storage devices. *J. Ind. Eng. Chem.* **2020**, *84*, 393–399. [[CrossRef](#)]
23. Shin, D.-Y.; Jo, H.-G.; Ahn, H.-J. Accelerating lithium storage capability of cobalt sulfide encapsulated within anion dual-doped mesoporous carbon nanofibers. *Appl. Surf. Sci.* **2020**, *527*, 146895–146903. [[CrossRef](#)]
24. Shin, D.-Y.; Sung, K.-W.; Ahn, H.-J. Synergistic effect of heteroatom-doped activated carbon for ultrafast charge storage kinetics. *Appl. Surf. Sci.* **2019**, *478*, 499–504. [[CrossRef](#)]
25. Li, S.; Wang, M.; Yao, Y.; Zhao, T.; Yang, L.; Wu, F. Effect of the Activation Process on the Microstructure and Electrochemical Properties of N-Doped Carbon Cathodes in Li–O₂ Batteries. *ACS Appl. Mater. Interfaces* **2019**, *11*, 34997–35004. [[CrossRef](#)] [[PubMed](#)]
26. Yu, K.; Lin, Y.; Fan, J.; Li, Q.; Shi, P.; Xu, Q.; Min, Y. Ternary N, S, and P-Doped Hollow Carbon Spheres Derived from Polyphosphazene as Pd Supports for Ethanol Oxidation Reaction. *Catalysts* **2019**, *9*, 114. [[CrossRef](#)]
27. Li, P.; Hwang, J.-Y.; Park, S.-M.; Sun, Y.-K. Superior lithium/potassium storage capability of nitrogen-rich porous carbon nanosheets derived from petroleum coke. *J. Mater. Chem. A* **2018**, *6*, 12551–12558. [[CrossRef](#)]
28. Hou, J.; Cao, C.; Idress, F.; Ma, X. Hierarchical Porous Nitrogen-Doped Carbon Nanosheets Derived from Silk for Ultrahigh-Capacity Battery Anodes and Supercapacitors. *ACS Nano* **2015**, *9*, 2556–2564. [[CrossRef](#)]
29. An, G.-H.; Jo, H.-G.; Ahn, H.-J. Surface effect of platinum catalyst-decorated mesoporous carbon support using the dissolution of zinc oxide for methanol oxidation. *Appl. Surf. Sci.* **2019**, *473*, 511–515. [[CrossRef](#)]
30. Xie, Y.; Yang, Y.; Zhou, Q.; Wang, L.; Yao, Y.; Zhu, X.; Fang, L.; Zhao, H.; Zhang, J. Metal-Free N, P-Codoped Porous Carbon Fibers for Oxygen Reduction Reactions. *J. Electrochem. Soc.* **2019**, *166*, 549–555. [[CrossRef](#)]
31. Jiang, H.; Zhu, Y.; Feng, Q.; Su, Y.; Yang, X.; Li, C. Nitrogen and Phosphorus Dual-Doped Hierarchical Porous Carbon Foams as Efficient Metal-Free Electrocatalysts for Oxygen Reduction Reactions. *Chem. Eur. J.* **2014**, *20*, 3106–3112. [[CrossRef](#)] [[PubMed](#)]
32. Lei, W.; Deng, Y.-P.; Li, G.; Cano, Z.P.; Wang, X.; Luo, D.; Liu, Y.; Wang, D.; Chen, Z. Two-Dimensional Phosphorus-Doped Carbon Nanosheets with Tunable Porosity for Oxygen Reactions in Zinc-Air Batteries. *ACS Catal.* **2018**, *8*, 2464–2472. [[CrossRef](#)]
33. Li, J.-C.; Hou, P.-X.; Cheng, M.; Liu, C.; Cheng, H.-M.; Shao, M. Carbon nanotube encapsulated in nitrogen and phosphorus co-doped carbon as a bifunctional electrocatalyst for oxygen reduction and evolution reactions. *Carbon* **2018**, *139*, 156–163. [[CrossRef](#)]
34. Yao, Z.; Fan, R.; Ji, W.; Yan, T.; Hu, M. N₈⁻ Polynitrogen Stabilized on Nitrogen-Doped Carbon Nanotubes as an Efficient Electrocatalyst for Oxygen Reduction Reaction. *Catalysts* **2020**, *10*, 864. [[CrossRef](#)]
35. Kim, J.-H.; Kannan, A.G.; Woo, H.-S.; Jin, D.-G.; Kim, W.; Ryu, K.; Kim, D.-W. A bi-functional metal-free catalyst composed of dual-doped graphene and mesoporous carbon for rechargeable lithium–oxygen batteries. *J. Mater. Chem. A* **2015**, *3*, 18456–18465. [[CrossRef](#)]
36. Balaish, M.; Jung, J.-W.; Kim, I.-D.; E-Eli, Y. A Critical Review on Functionalization of Air-Cathodes for Nonaqueous Li–O₂ Batteries. *Adv. Funct. Mater.* **2020**, *30*, 1808303–1808336. [[CrossRef](#)]
37. Gallant, B.M.; Mitchell, R.R.; Kwabi, D.G.; Zhou, J.; Zuin, L.; Thompson, C.V.; Shao-Horn, Y. Chemical and Morphological Changes of Li–O₂ Battery Electrodes upon Cycling. *J. Phys. Chem. C* **2012**, *116*, 20800–20805. [[CrossRef](#)]
38. Gao, K.; Wang, B.; Tao, L.; Cunnning, B.V.; Zhang, Z.; Wang, S.; Ruoff, R.S.; Qu, L. Efficient Metal-Free Electrocatalysts from N-Doped Carbon Nanomaterials: Mono-Doping and Co-Doping. *Adv. Mater.* **2019**, *31*, 1805121–1805131. [[CrossRef](#)]
39. Zhao, Z.; Gao, C.; Mac, K.; Lu, Y. Pyrolysis derived helically nitrogen-doped carbon nanotubes with uniform cobalt for high performance oxygen reduction. *Appl. Surf. Sci.* **2020**, *504*, 144380–144385. [[CrossRef](#)]
40. Zhang, J.; Wang, J.; Wu, Z.; Wang, S.; Wu, Y.; Liu, X. Heteroatom (Nitrogen/Sulfur)-Doped Graphene as an Efficient Electrocatalyst for Oxygen Reduction and Evolution Reactions. *Catalysts* **2018**, *8*, 475. [[CrossRef](#)]
41. Nunes, M.; Rocha, I.M.; Fernandes, D.M.; Mestre, A.S.; Moura, C.N.; Carvalho, A.P.; Pereira, M.F.R.; Freire, C. Sucrose-derived activated carbons: Electron transfer properties and application as oxygen reduction electrocatalysts. *RSC Adv.* **2015**, *5*, 102919–102931. [[CrossRef](#)]
42. An, G.-H.; Lee, Y.-G.; Ahn, H.-J. Multi-active sites of iron carbide nanoparticles on nitrogen@cobalt-doped carbon for a highly efficient oxygen reduction reaction. *J. Alloy. Compd.* **2018**, *746*, 177–184. [[CrossRef](#)]
43. Lee, Y.-G.; Ahn, H.-J. Tri(Fe/N/F)-doped mesoporous carbons as efficient electrocatalysts for the oxygen reduction reaction. *Appl. Surf. Sci.* **2019**, *487*, 389–397. [[CrossRef](#)]

44. Sun, J.; Wang, S.; Wang, Y.; Li, H.; Zhou, H.; Chen, B.; Zhang, X.; Chen, H.; Qu, K.; Zhao, J. One Simple Strategy towards Nitrogen and Oxygen Codoped Carbon Nanotube for Efficient Electrocatalytic Oxygen Reduction and Evolution. *Catalysts* **2019**, *9*, 159. [[CrossRef](#)]
45. Marsudi, M.A.; Ma, Y.; Prakoso, B.; Hutani, J.J.; Wibowo, A.; Zong, Y.; Liu, Z.; Sumboja, A. Manganese Oxide Nanorods Decorated Table Sugar Derived Carbon as Efficient Bifunctional Catalyst in Rechargeable Zn-Air Batteries. *Catalysts* **2020**, *10*, 64. [[CrossRef](#)]
46. Ryu, W.-H.; Yoon, T.-H.; Song, S.H.; Jeon, S.; Park, Y.-J.; Kim, I.-D. Bifunctional Composite Catalysts Using Co₃O₄ Nanofibers Immobilized on Nonoxidized Graphene Nanoflakes for High-Capacity and Long-Cycle Li–O₂ Batteries. *Nano Lett.* **2013**, *13*, 4190–4197. [[CrossRef](#)]
47. Xie, L.; Zhao, D.; Dai, J.; Wu, Z.; Li, L. Solvothermally Doping NiS₂ Nanoparticles on Carbon with Ferric Ions for Efficient Oxygen Evolution Catalysis. *Catalysts* **2019**, *9*, 458. [[CrossRef](#)]
48. Liu, X.; Chen, C.; Cheng, Q.; Zou, L.; Zou, Z.; Yang, H. Binary Nitrogen Precursor-Derived Porous Fe-N-S/C Catalyst for Efficient Oxygen Reduction Reaction in a Zn-Air Battery. *Catalysts* **2018**, *8*, 158. [[CrossRef](#)]

Publisher’s Note: MDPI stays neutral with regard to jurisdictional claims in published maps and institutional affiliations.



© 2020 by the authors. Licensee MDPI, Basel, Switzerland. This article is an open access article distributed under the terms and conditions of the Creative Commons Attribution (CC BY) license (<http://creativecommons.org/licenses/by/4.0/>).